XMM-Newton observations of the Galactic Centre Region - I: The distribution of low-luminosity X-ray sources

V. Heard[1*] and R. S. Warwick[1]

[1]*Department of Physics and Astronomy, University of Leicester, University Road, Leicester, UK*

ABSTRACT

We exploit *XMM-Newton* archival data in a study of the extended X-ray emission emanating from the Galactic Centre (GC) region. *XMM-Newton* EPIC-pn and EPIC-MOS observations, with a total exposure time approaching 0.5 and 1 Ms respectively, were used to create mosaiced images of a 100 pc × 100 pc region centred on Sgr A* in four bands covering the 2–10 keV energy range. We have also constructed a set of narrow-band images corresponding to the neutral iron fluorescence line (Fe I Kα) at 6.4 keV and the K-shell lines at 6.7 keV and 6.9 keV from helium-like (Fe XXV Kα) and hydrogenic (Fe XXVI Lyα) iron ions. We use a combination of spatial and spectral information to decompose the GC X-ray emission into three distinct components. These comprise: firstly the emission from hard X-ray emitting unresolved point sources; secondly the reflected continuum and fluorescent line emission from dense molecular material; and, thirdly, the soft diffuse emission from thermal plasma in the temperature range, $kT \approx 0.8$–1.5 keV.

We show that the unresolved-source component accounts for the bulk of the 6.7-keV and 6.9-keV line emission and also makes a major contribution to both the 6.4-keV line emission and the 7.2–10 keV continuum flux. We fit the observed X-ray surface brightness distribution with an empirical 2-d model, which we then compare with a prediction based on an NIR-derived 3-d mass model for the old stellar population in the GC. The X-ray surface brightness falls-off more rapidly with angular offset from Sgr A* than the mass-model prediction. One interpretation is that the 2–10 keV X-ray emissivity increases from $\approx 5 \times 10^{27}$ erg s^{-1} M$_\odot$$^{-1}$ at 20′ up to almost twice this value at 2′. Alternatively, some refinement of the mass model may be required, although it is unclear whether this applies to the Nuclear Stellar Cluster, the Nuclear Stellar Disc, or a combination of both components.

The unresolved hard X-ray emitting source population, on the basis of spectral comparisons, is most likely dominated by magnetic cataclysmic variables, primarily intermediate polars. We use the X-ray observations to set constraints on the number density of such sources at angular offsets between $2' - 20'$ from Sgr A* (projected distances at the GC of 4.6–46 pc). Our analysis does not support the conjecture that a significant fraction of the hard X-ray emission from the GC originates in very-hot (~ 7.5 keV) *diffuse* thermal plasma.

Key words: Galaxy: centre – X-rays: ISM, binaries

1 INTRODUCTION

The centre of our Galaxy represents an intriguing laboratory for the study of high energy processes and interactions. Within the central 100 pc, the rise in the stellar mass density is complemented by a concentration of gaseous, largely molecular matter, in a region known as the Central Molecular Zone (Morris & Serabyn 1996). Recent star formation coupled with supernova explosions every few thousand years serve to inject high-energy particles into the mix, which power non-thermal emission and drive outflows (Crocker et al. 2011; and references therein). At its heart, our Galaxy hosts a currently-quiescent supermassive black hole, Sgr A*, with a mass of 4×10^6 M$_\odot$ (Schödel et al. 2002; Ghez et al. 2008). Quite plausibly recent activity on Sgr A* may also have energised the sur-

* E-mail: vh41@le.ac.uk

rounding region (Sunyaev & Churazov 1998; Koyama et al. 1996; Murakami et al. 2000; Ponti et al. 2010; Capelli et al. 2012). Given this context, it is not surprising that, even when the contribution of highly-luminous X-ray binaries and transients is excluded, the central region of our Galaxy exhibits a rich variety of both compact X-ray sources and diffuse X-ray emission (*e.g.*, Muno et al. 2004a; Park et al. 2004; Wang et al. 2006; Muno et al. 2008, 2009).

One focus of research over the last forty years has been the nature of the unresolved hard X-ray emission, known as the Galactic Ridge X-ray Emission (GRXE), which can be traced along the Galactic Plane, reaching a maximum surface brightness at the GC (Worrall & Marshall 1983; Warwick et al. 1985; Koyama et al. 1986, 1989; Revnivtsev et al. 2006). This unresolved X-ray emission is known to exhibit many K-shell emission lines from highly-ionised atoms, with the most prominent of these lines being He-like (Fe XXV Kα) and H-like (Fe XXVI Lyα) iron at 6.7 and 6.9 keV respectively. The flux ratio of Fe XXV Kα/Fe XXVI Lyα suggests the origin is in optically-thin thermal plasma emission at a temperature $\sim$ 7.5 keV (e.g., Koyama et al. 1986; Koyama et al. 2007a; Yamauchi et al. 2009). If this emission is diffuse in nature, its temperature is too high for it to remain gravitationally bound to the Galactic Plane and it would instead escape with a velocity exceeding 1000 km s^{-1} (Worrall & Marshall 1983; Koyama et al. 1986). The kinetic energy required to sustain the plasma ($\sim 10^{42}$ erg s^{-1}), is equivalent to the occurrence of at least one supernova explosion every thirty years (Kaneda et al. 1997; Yamasaki et al. 1997). This far exceeds current estimates of the supernova rate within the region. Furthermore, the spectra of supernova remnants (SNRs) exhibit thermal plasma components with temperatures typically in the range of $kT \sim$ 0.2–0.8 keV and seldom, if ever, with $kT > 3$ keV. These difficulties call into question whether the emission can be truly diffuse in nature.

Early *Chandra* deep-field observations revealed a large population of faint point sources within the GC region (Wang et al. 2002; Muno et al. 2003). More recently, Revnivtsev et al. (2009) have reported that within a particular deep-field observation ($l_{\text{II}}, b_{\text{II}} = +0.08°, -1.42°$), more than $\sim$ 80 per cent of the continuum and line emission around 6.7 keV can be resolved into point sources. A high concentration of discrete sources is perhaps to be expected, given that the central $2° \times 0.8°$ region of the Milky Way contains $\sim$ 1 per cent of the Galactic mass (Launhardt et al. 2002). In fact, Muno et al. (2006) compared the spatial distribution of the X-ray emission from point sources with the stellar mass distribution model derived from the *NIR* map of Launhardt et al. (2002) and, within the limits of the statistics, found a good correlation between them. They conclude that the majority of point sources with $L_{\text{X}} \leqslant 10^{34}$ erg s^{-1} are likely to be magnetic cataclysmic variables (CVs). In such systems, an accretion shock is generated above the white dwarf surface, which heats the accreting material to temperatures $kT > 15$ keV. The resulting highly-ionised, optically-thin plasma cools and, eventually, settles onto the white dwarf. The resulting X-ray spectrum comprises a complex blend of contributions generated at differing temperatures, densities and optical depths (e.g., Cropper et al. 1999; Yuasa et al. 2010). As well as a hard continuum, the X-ray spectra of magnetic CVs are characterised by a complex of iron-K lines including strong He-like, H-like and fluorescent components, the latter arising from relatively cold iron in states from Fe I to XVII (Hellier & Mukai 2004). Support for the conjecture that magnetic CVs represent an important GC source population also comes from studies of the hard X-ray emitting, low-luminosity X-ray source population found locally in our Galaxy (Sazonov et al. 2006); and the distribution of the GRXE across the central quadrants of the Galactic Plane (Revnivtsev et al. 2006).

Uchiyama et al. (2011) recently investigated the Fe XXV Kα emission from both the Galactic Ridge and GC regions using *Suzaku* data and compared the spatial profiles of the line emission with the stellar mass distribution models considered by Muno et al. (2006). They concluded that the distribution of the line emission along the Galactic Ridge is consistent with an unresolved point source origin but argued that an additional component is required to account for the excess emission seen within the GC region. In contrast, based on a detailed spectral analysis of *Suzaku* observations in the Galactic bulge region, Yuasa et al. (2012) concluded that virtually all of the unresolved X-ray emission could be explained in terms of the integrated emission of two point source components, magnetic accreting white dwarfs, which give rise to the hard emission extending from 5–50 keV, and stellar coronal sources which might account for the softer (kT 1.2–1.5 keV) thermal emission evident in the bulge fields.

In this paper, we report on a detailed investigation of the spatial and spectral characteristics of the X-ray emission observed within the central 100 parsecs of the Galaxy based on data from *XMM-Newton*. The emphasis of our study is on constraining the model for the unresolved, hard X-ray emitting sources and setting limits on what fraction of the emission might reasonably be described as diffuse in nature. In the next section, we give details of the *XMM-Newton* observations selected for this analysis and the procedures followed in the data reduction. We also describe the techniques employed to construct mosaiced X-ray images covering a range of broad and narrow energy bands and to extract representative X-ray spectra. In §3 we outline how the spatial and spectral information can be modelled in terms of three distinct emission components. We then discuss in §4 the contribution that unresolved low-luminosity sources make to the GC X-ray emission and whether, in light of our results, there is any requirement for truly diffuse, very-hot thermal plasma emission in the GC. Finally §5 gives a brief summary of our conclusions. Throughout this work, the distance to the GC is assumed to be 8 kpc (Gillessen et al. 2009).

2   OBSERVATIONS AND DATA REDUCTION

The *XMM-Newton* Science Archive (XSA) was used to select observations, publicly available as of 2011 July, with pointing positions within 0.7° of ($l_{\text{II}}, b_{\text{II}}$) = (0°, 0°). A minimum effective exposure of 1000 s in at least one of the three EPIC instruments (Strüder et al. 2001; Turner et al. 2001) was set as a requirement. Similarly only observations with at least one of the EPIC cameras operating in either full-frame (FF) or extended full-frame (EFF) mode were considered. The majority of the observations were carried out using the

medium filter, although either the thin or thick filter were deployed in some instances. Table 1 provides a summary of the set of *XMM-Newton* observations used in the current analysis and related information.

The data reduction was based on SAS v11.0 (hereafter, SAS). For every observation listed in Table 1, the Observation Data Files for each of the EPIC instruments, pn, MOS-1 and MOS-2, were reprocessed using the SAS tasks EPCHAIN and EMPROC. Each dataset was screened for periods of soft proton flaring through the creation of full-field light curves for the energy range 10–12 keV (utilising only single-pixel events). Good Time Interval (GTI) selections were made by setting a suitable threshold for each instrument, chosen to filter out those periods when the instrument background count rate was highly variable and clearly in excess of the local quiescent level. The resulting exposure times for each instrument after the application of the GTI filtering are reported in Table 1. The total "live" time summed over the set of 50 pn observations and the 56 MOS-1/MOS-2 observations was, respectively, ≈ 0.5 and ≈ 0.95 Ms. The event lists were filtered so as to include only single- and double-pixel events for pn (PATTERN<=4) and up to quadruple-pixel events for MOS-1 and MOS-2 (PATTERN<=12). Out-of-Time (OoT) events have a non-negligible impact on pn data and appropriate corrections were applied. As a preliminary step, the SAS task EPCHAIN was used to generate OoT event lists, filtered in an identical way to the primary datasets.

2.1 Construction of the image mosaics

Images from each observation and from each camera were constructed in four "broad" bands covering the 2–10 keV bandpass (see Table 2). Instrument exposure maps were also made for each of these bands. In the case of the pn data, events with energies in the range 7.8–8.3 keV (which encompasses the prominent copper Kα instrumental line) were excluded when constructing the very-hard band image. Similarly for the MOS very-hard band, events in the 9.0–10.0 keV range were discarded (since the MOS response rapidly declines in this energy range).

Images were also made in a number of narrow bands encompassing prominent Fe-K spectral lines. Table 2 lists the energy ranges used in the present study corresponding to the neutral (or near-neutral) iron fluorescence line (Fe I Kα) at 6.4 keV and the K-shell lines at 6.7 keV and 6.9 keV from He-like (Fe XXV Kα) and hydrogenic (Fe XXVI Lyα) ions of iron. Two narrow bands sampling the "continuum" at energies immediately below and above the iron-line complex were also utilised (see Fig. 1).

The first correction applied to the pn images involved the construction of a set of OoT images (one per band) from the OoT event lists. These OoT images were scaled to the estimated OoT event fraction (6.3 and 2.3 per cent in FF and EFF modes respectively) and subtracted from the raw pn image using the FTOOLS task FARITH (FTOOLS v6.11, Blackburn 1995).

The interactions of high-energy cosmic-ray particles, with the EPIC detectors are known to give rise to an instrumental background consisting of both a hard continuum and fluorescent line features (Lumb et al. 2002). A correction for the instrumental background was applied to both the pn and MOS images by making use of EPIC filter wheel

Table 1. Details of the *XMM-Newton* observations used in this work. All observations were made with a Medium filter in place unless otherwise stated.

| ObsID	Observation date	Exposure time (s)		
		MOS-1	MOS-2	pn
0112970701	2000-09-11	23110	23116	16951
0112970401	2000-09-19	22871	22671	13712
0112970501	2000-09-21	14650	14758	4716
0112971001	2000-09-24	8500	8898	7356[†]
0112971501	2001-04-01	6205	7242	2929
0112971901	2001-04-01	5215	5804	1339
0112972101	2001-09-04	22500	22515	16447
0111350101	2002-02-26	38944	39164	31139[†]
0111350301	2002-10-03	8074	8097	5914[†]
0202670501	2004-03-28	26554	29254	9064
0202670601	2004-03-30	34440	37048	24267
0202670701	2004-08-31	81716	84000	38114
0202670801	2004-09-02	102082	106098	62475
0302882501	2006-02-27	8167	8407	4595
0302882601	2006-02-27	2858	3153	966
0302882701	2006-02-27	4892	5097	-
0302882801	2006-02-27	7167	7072	2231
0302882901	2006-02-27	6667	6575	1876
0302883001	2006-02-27	6764	6268	-
0302883101	2006-02-27	10491	10101	1593
0302883201	2006-03-29	6132	6138	2541
0302883901	2006-09-08	6380	6285	2366
0302884001	2006-09-08	6377	6389	3319
0302884101	2006-09-08	6074	5683	1225
0302884201	2006-09-08	6480	6086	4363
0302884301	2006-09-09	6379	6181	4014
0302884401	2006-09-09	5440	5145	2748
0302884501	2006-09-09	8154	7763	5065
0506291201	2007-02-27	24438	19010	-
0402430701	2007-03-30	30390	29680	8827
0402430301	2007-04-01	52528	42381	16728
0402430401	2007-04-03	36809	31887	15841
0504940101	2007-09-06	6323	5918	2831
0504940201	2007-09-06	9696	9588	-
0504940401	2007-09-06	6117	6227	4396
0504940501	2007-09-06	5912	5929	4050
0504940601	2007-09-06	3552	3061	-
0504940701	2007-09-06	6419	5726	3355
0511000101	2008-03-03	1582[‡]	1781[‡]	-
0511000301	2008-03-03	5431[‡]	5238[‡]	606[‡]
0511000501	2008-03-04	6020[‡]	6229[‡]	1528[‡]
0511000701	2008-03-04	6422[‡]	5828[‡]	2825[‡]
0511000901	2008-03-04	6028[‡]	4828[‡]	4303[‡]
0511001101	2008-03-04	6518[‡]	6529[‡]	4352[‡]
0511001301	2008-03-04	4730[‡]	2950[‡]	2342[‡]
0505870301	2008-03-09	12275	12073	4704
0505670101	2008-03-23	79223	73233	44097
0511000201	2008-09-23	6319[‡]	6325[‡]	3856[‡]
0511000401	2008-09-23	3688[‡]	2481[‡]	3682[‡]
0511000601	2008-09-23	6518[‡]	6328[‡]	4198[‡]
0511000801	2008-09-27	6409[‡]	6224[‡]	1931[‡]
0511001001	2008-09-27	6518[‡]	6529[‡]	4352[‡]
0511001201	2008-09-27	6518[‡]	3522[‡]	722[‡]
0554750401	2009-04-01	28142	20968	24703
0554750501	2009-04-03	41733	39752	27885
0554750601	2009-04-05	36523	34838	23601
Total time:		942464	910071	487036

[†] Thick filter deployed.
[‡] Thin filter deployed.

Table 2. Energy ranges (in keV) of the four broad bands covering the full $2-10$ keV bandpass and of the narrow bands encompassing the three spectral lines of iron.

Broad bands	
Medium	$2.0 - 4.5$
Hard	$4.5 - 6.0$
Iron	$6.0 - 7.2$
Very-hard	$7.2 - 10.0$¶
Narrow bands	
Continuum-low	$5.70 - 6.15$
Fe I Kα	$6.270 - 6.510$
Fe XXV Kα	$6.525 - 6.825$
Fe XXVI Lyα	$6.840 - 7.110$
Continuum-high	$7.20 - 7.65$

¶The $7.8 - 8.3$ keV spectral region encompassing the Cu Kα instrumental line was excluded in the case of the pn data, whereas for the MOS data the very-hard band was truncated at 9.0 keV.
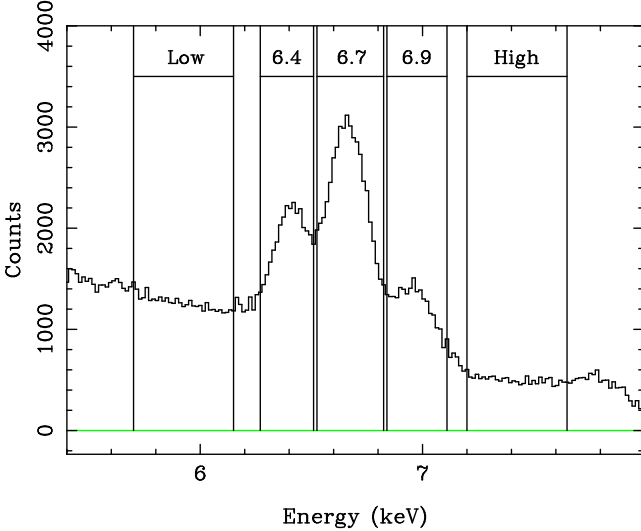
Figure 1. The full-field spectrum from the pn camera (ObsID: 0202670801) in the region of the Fe-K lines. The underlying continuum was sampled in two narrow bands (marked "Low" and "High") at energies immediately below and above the Fe-K complex. The various narrow bands are delineated by the vertical lines.

closed (FWC) data obtained from the background analysis website maintained by ESA[1]. With the sky signal blocked, the FWC exposures provide a relatively clean measure of the instrumental background and, therefore, may be used to model and subtract the instrument background. Merged event files containing all available FWC data were selected for both the pn FF (Rev. 266–Rev. 2027) and pn EFF (Rev. 355–Rev. 1905) modes. Merged FWC event files for the MOS cameras in FF mode were also obtained with the caveat that the FWC data for MOS-1 were split into two categories: before (Rev. 231–Rev. 961) and after (Rev. 961–Rev. 2027) the failure of CCD-6 on 2005 March 9. The MOS-2 FWC event list contained data taken from Rev. 230–Rev. 2027. Using the SKYCAST software, the FWC data (initially in detec-

Table 3. Factors (f) used in interpolating between the continuum-low and continuum-high narrow band measurements to give the continuum underlying the line image.

Line	pn	MOS
Fe 6.4-keV	0.72	0.64
Fe 6.7-keV	0.53	0.435
Fe 6.9-keV	0.325	0.245

Table 4. Percentage spillover from one iron-line band to another as a result of the limited spectral resolution of the EPIC cameras.

	pn	MOS
Fe 6.4-keV to Fe 6.7-keV	8.5	2.7
Fe 6.4-keV to Fe 6.9-keV	5.0	4.1
Fe 6.7-keV to Fe 6.4-keV	2.2	1.9

tor coordinates) were cast into images in the sky-coordinate frame applicable to the particular observation. The number of counts measured in the corners of the detector (*i.e.*, the regions of the detector shielded from the sky) in the actual observation were then divided by the equivalent number of counts in the FWC image to give a FWC scale factor for each band, instrument, and observation. A correction for the instrument background was then applied to each observation by subtracting the scaled FWC image.

As a final step prior to the combining of the images into a mosaic, the images were inspected visually for undesirable artefacts such as scattered light features and bright transient sources. These artefacts were spatially masked when encountered and a corresponding correction applied to the exposure maps.

In the production of the image mosaics, observation 0202670801 (centred at RA, Dec of 266.4413°, -29.028972°) was used as a reference field. In the case of the pn camera, the image data deriving from all the other observations were resampled and co-added to the reference image. This process was repeated for each band and also for each exposure map. Flat-fielding then involved dividing each co-added image by the appropriate co-added exposure map. For the narrow-band images we used the co-added 6.0–7.2 keV exposure map in this flat-fielding step. The same process was used for the MOS datasets, although in this case the MOS-1 and MOS-2 image data and exposure maps were combined prior to the flat-fielding step. The resulting mosaiced images have a format of 648×648 pixels ($4''$ pixels) corresponding to a $43.2' \times 43.2'$ field. At the distance of the GC this field size covers a projected extent of 100×100 pc.

The upper-left panel of Fig. 2 shows the 2.0–10.0 keV pn mosaic produced by summing the four broad-band images. The corresponding exposure map is shown in the upper-right panel. Fig. 2 (lower-left panel) also presents a blow-up of the region to the north-east of Sgr A*, where there is extended high surface brightness X-ray emission.

In order to trace the distribution of the iron-line emission, it is necessary to make a correction to the narrow-band images for the in-band continuum emission underlying the emission lines. Here the approach was to calculate an interpolated "continuum" image by multiplying the narrow-band continuum-low and -high images (see Table 2) by a factor f
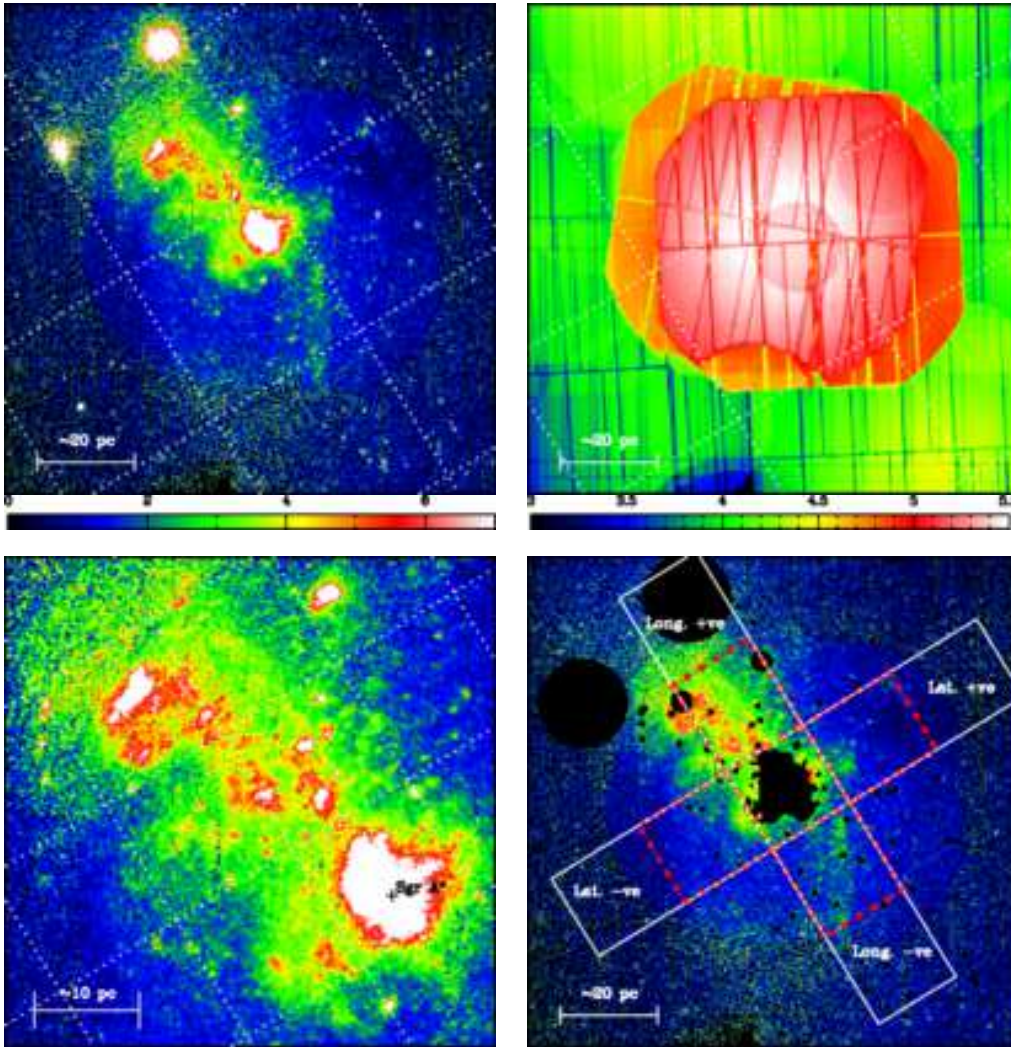
Figure 2. Image mosaics based on *XMM-Newton* observations covering a central $43.2' \times 43.2'$ field (100×100 pc at the GC). The images are constructed on a celestial coordinate grid with east to the left. *Upper-left panel:* 2–10 keV pn image. The adjacent colour bar is calibrated in units of pn counts per pixel per 20 ks. *Upper-right panel:* The corresponding pn exposure map. The adjacent colour bar is calibrated in units of $\log_{10}$ of the exposure (sec). *Lower-left panel:* A blow-up of the 2–10 keV image showing the region to the north-east of Sgr A*. *Lower-right panel:* The 2–10 keV pn image overlaid by a spatial mask which removes the most luminous sources (see §2.2). The longitudinal and latitudinal spatial cuts are represented by the two intersecting white rectangles, which have long-axis dimensions of $\pm22'$ and full widths of $8'$ (see §2.3). The red boxes (of dimension $8' \times 9'$) define the four regions from which spectral data were extracted (see §2.4). In three of the panels the white dotted lines represent a Galactic coordinate grid with a $15'$ spacing.

and $1 - f$ respectively, and then summing the two products. Full-field spectra extracted from a number of the GC observations (see Fig. 1) were used to estimate appropriate values of f for the three Fe-lines, for both the pn and MOS channels (see Table 3). Continuum-subtracted line images were produced by subtracting the resultant interpolated continuum images from the line images (with the former scaled so as to account for the different bandpasses of the narrow-band line and continuum images.

The need for a further correction to the line images arises due to the limited spectral resolution of the pn and MOS cameras. This results in some spillover of signal from a given iron line into the adjacent line band or bands (see Fig. 1). Here we used the X-ray spectral-fitting package (XSPEC, v12.6.0) to estimate the spillover factors for spectra dominated either by reflection or hot-thermal emission. The for-

mer may be modelled as a bright Fe I Kα line at 6.4 keV plus an associated Fe I Kβ line at 7.11 keV (with 11 per cent of the Kα normalisation) superimposed on a power-law continuum with spectral slope $\Gamma \approx 1.7$. Our simulations showed that the two reflection lines contaminate the 6.7-keV and 6.9-keV narrow-bands as summarised in the first two lines of Table 4 (separate values are quoted for the pn and MOS instruments since their spectral resolution and energy response differ). Similarly, the spillover of the 6.7-keV He-like Fe Kα emission into the 6.4-keV narrow-band was simulated using was a solar-abundance `apec` model with the plasma temperature set at $kT = 7.5$ keV (Smith et al. 2001); the results are given in the third line in Table 4. Final Fe-line images were produced by subtracting appropriate fractions of the other line images. Hereafter, we will often refer to the

Fe I Kα, Fe XXV Kα and Fe XXVI Lyα lines simply as the 6.4-keV, 6.7-keV and 6.9-keV lines, respectively.

Fig. 3 shows the pn continuum-subtracted images for the three iron lines. The lower-right panel of Fig. 3 also shows the very-hard (7.2–10.0 keV) band image. Note that all of these images have been heavily smoothed with a circular Gaussian function of width $\sigma = 5$ pixels. The brightest 6.4-keV line emission is concentrated to the north-east of Sgr A* in a region with a high molecular cloud density (Koyama et al. 1996; Park et al. 2004; Ponti et al. 2010; Capelli et al. 2011). In contrast, the surface brightness in the 6.7-keV and 6.9-keV iron-line images show a smooth increase towards Sgr A*, as might be expected if these lines arise predominantly in the integrated emission of unresolved point sources (Muno et al. 2006, 2009; Revnivtsev et al. 2007; Hong et al. 2009). On the other hand, the very-hard band image can be readily interpreted in terms of a combination of the two emission distributions noted previously.

2.2 Spatial masking of point sources

The presence of luminous point sources within the field of view introduces a degree of confusion noise into the images, which can be removed via spatial masking. In order to produce such a spatial mask, a catalogue of sources was constructed based on the Second *XMM-Newton* Serendipitous Source Catalogue (the 2XMMi catalogue; Watson et al. 2009). Specifically, 2XMMi sources within the GC field with 2.0–12.0 keV flux greater than $\sim 1.5 \times 10^{-13}$ erg s^{-1} cm^{-2} were included in a preliminary source list. The mosaiced images were then inspected at the source locations and a number of possibly spurious sources discarded. Conversely, a small number of sources not included in the 2XMMi catalogue, but clearly visible in the images, were added manually to the list. The result was a catalogue of 84 sources. A spatial mask was then made by excising circular regions of radius $25''$ at each source position (corresponding to the removal of roughly 80 per cent of the source response). Larger excision circles were used for two very bright sources to the north-east of Sgr A*, for the Arches cluster and for the pulsar wind nebula, G0.13-0.11. We also excluded the brightest regions of the Sgr A East complex (using a contour based on its 6.7-keV Fe-line emission). The full mask array was then applied to every image employed in our study prior to any smoothing; the lower-right panel of Fig. 2 shows the result in the case of the 2–10 keV pn image.

2.3 Spatial cuts

Our investigation of the various components of the diffuse X-ray emission present in the GC requires both a spatial and spectral modelling approach. We based our spatial modelling on cuts through the various images in Galactic longitude and latitude centred on the position of Sgr A*. The white rectangles in Fig. 2 (lower-right panel) indicate the regions of the mosaiced images which were thereby sampled. The cuts extend out to offset angles of $\pm 22'$ with a $\pm 4'$ extent perpendicular to the cut axis. The spatial resolution along each cut is $1'$. We excluded segments of the cuts for which more than half the area was already excluded by the source mask. This resulted in the loss of the central $\pm 2'$ region

(which is confused by Sgr A East) in both cuts and the eastern-most $4'$ section of the longitudinal cut. The results from this analysis are presented in §3.3.

2.4 Spectral extraction

X-ray spectra were extracted from four regions within the central 100 pc zone, corresponding to the sky areas sampled by the spatial cuts at offsets from Sgr A* of between $4'$ and $13'$ (see the lower-right panel of Fig. 2). The dimensions of each region are therefore $8' \times 9'$, with the longer axis orientated along the cut direction. Luminous point sources were excluded from the extracted regions corresponding to those masked out in §2.2.

For simplicity, we extracted the spectra from a single pn observation (0202670801) for which the exposure time after GTI-filtering was ~ 62 ks. The wide extent of the diffuse emission in the GC field makes the selection of a background region for use in spectral analysis problematic. We opted, therefore, to determine the background spectra from the appropriate FWC dataset. FWC spectra were selected from geometrical areas on the detector matching those of the four sky regions. A simple scaling of the FWC spectrum so as to match the sky exposure then proved adequate as the instrumental background. Subsequent spectral analysis then requires all the relevant GC emission components as well as the cosmic X-ray background (CXB) to be included in the spectral model (see §3.4). The SAS tools ARFGEN and RMFGEN were also used to produce the appropriate auxiliary response and response matrix files. The spectra were grouped so that each contained at least ten counts per bin.

3 SPATIAL AND SPECTRAL MODELLING OF THE GC EMISSION

3.1 Distinct emission components

A number of unresolved X-ray emitting components are evident in the GC region, which can be distinguished by virtue of their distinctive spatial and spectral characteristics. Here, for simplicity, we attempt to model this emission in terms of just three major components.

The first is the emission associated with the unresolved hard X-ray emitting point sources. In the present analysis we have masked out the sources brighter than 1.5×10^{-13} erg s^{-1} cm^{-2} in the 2–12 keV band which, at the distance of the GC, corresponds to a 2–10 keV X-ray luminosity threshold of $\approx 10^{33}$ erg s^{-1}. Hence here we are dealing with the integrated emission of sources less luminous than this. Our spectral description of this component is in terms of a hard continuum (taken to be thermal bremsstrahlung with $kT = 7.5$ keV) with associated Fe-line emission at 6.4, 6.7 and 6.9 keV (*i.e.* neutral, He-like and H-like iron Kα emission). We assume that unresolved sources give rise to the bright central concentration of emission, which is most clearly discerned in the 6.7-keV and 6.9-keV images (Fig. 3).

The second major emission component observed in the GC is that associated with dense molecular clouds. The most obvious signature is the iron fluorescence line at 6.4 keV (Koyama et al. 2007b, 2009; Park et al. 2004; Ponti et al.
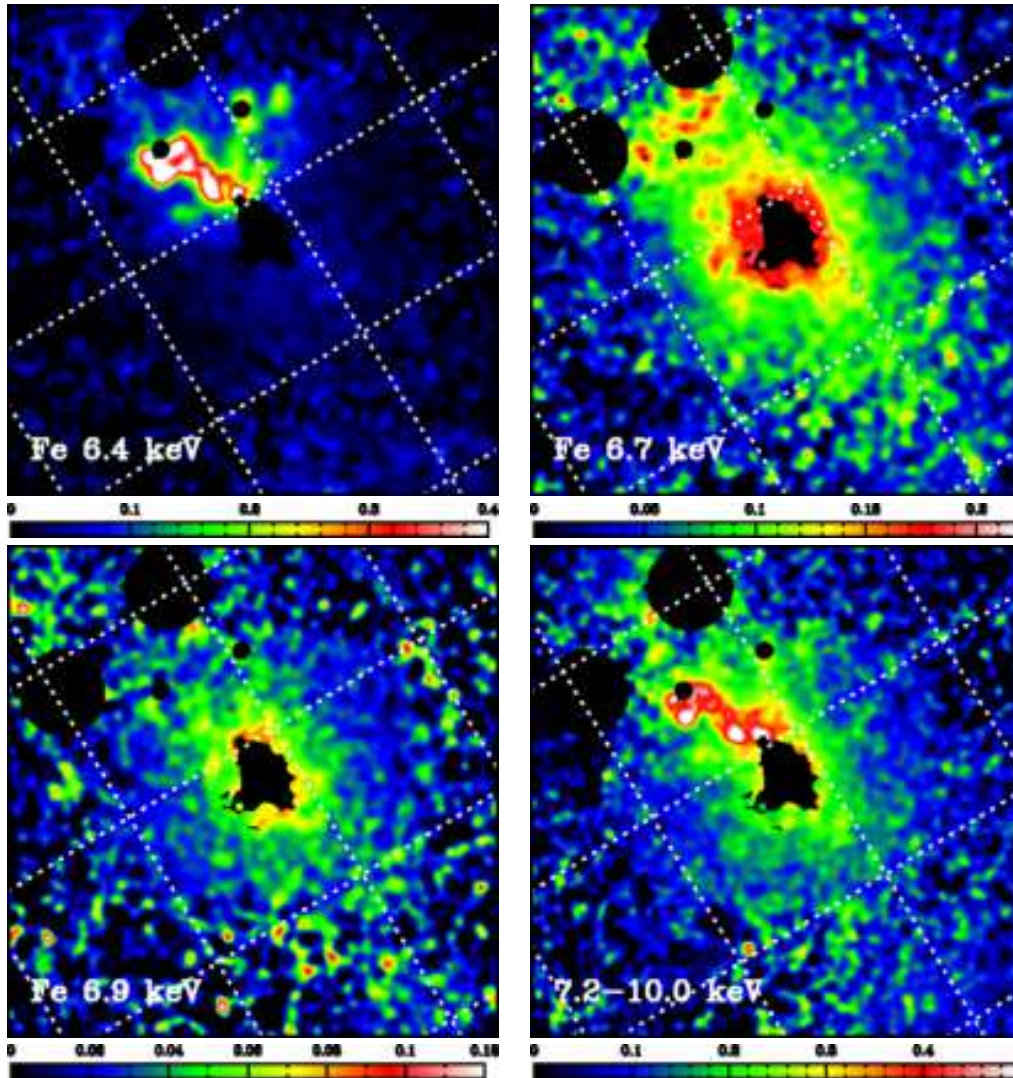
Figure 3. The distribution of iron-line emission and the associated very-hard continuum in the central 100 pc of the Milky Way. *Upper-left panel:* the neutral iron fluorescence line at 6.4 keV. *Upper-right panel:* the He-like iron line (Fe XXV Kα) at 6.7 keV. *Lower-left panel:* the H-like iron line (Fe XXVI Lyα) at 6.9 keV. *Lower-right panel:* the very-hard (7.2–10 keV) band image. All four images have been smoothed with a Gaussian mask function of width $\sigma = 5$ pixels. The adjacent colour bars are calibrated in units of pn counts per pixel per 20 ks. The white dotted lines represent a Galactic coordinate grid with a $15'$ spacing.

2010; Capelli et al. 2012). This fluorescence is very likely excited by hard X-ray illumination of the clouds. The Thomson scattering of the incident X-ray flux back into our line-of-sight gives rise to a second spectral characteristic, namely the presence of a hard power-law X-ray continuum (with photon index Γ in the range 1.5–2.0). Dense molecular material is known to be very unevenly distributed in the GC with a concentration to the north-east of Sgr A* (*e.g.,* Tsuboi et al. 1999). This explains the highly asymmetric surface brightness distribution seen in the 6.4-keV image, which is also reproduced in the very-hard band image (see Fig. 3).

A third emitting component is that arising from diffuse thermal plasma, most likely energised by recent supernova explosions and, in some localised regions, by the colliding stellar winds of massive stars. This relatively soft emission component is pervasive throughout the GC region; however, the highest surface brightness region outside of the central few arcmins, where emission associated with the Central Cluster and the Sgr A East SNR dominates (Baganoff et al. 2003; Muno et al. 2004b), is again located to the north-east of Sgr A*, where the density of molecular material is high. The temperature and, possibly, metal abundance of this soft thermal plasma may vary with location. In modelling this component we assume that the thermal structure can be adequately represented by two temperature components, one at $kT \approx 0.8$ keV and the other at $kT \approx 1.5$ keV. The former accounts for much of the line emission evident in the X-ray spectrum of the GC region below ~ 4 keV, the most prominent spectral line being the Kα line of He-like sulphur at 2.4 keV. The 1.5-keV component, whilst also contributing significantly to the spectrum below 4 keV, is hot enough to produce 6.7-keV iron-line emission.

This paper focuses on an investigation of the spatial distribution and spectral characteristics of the emission associated with the unresolved point source population. An
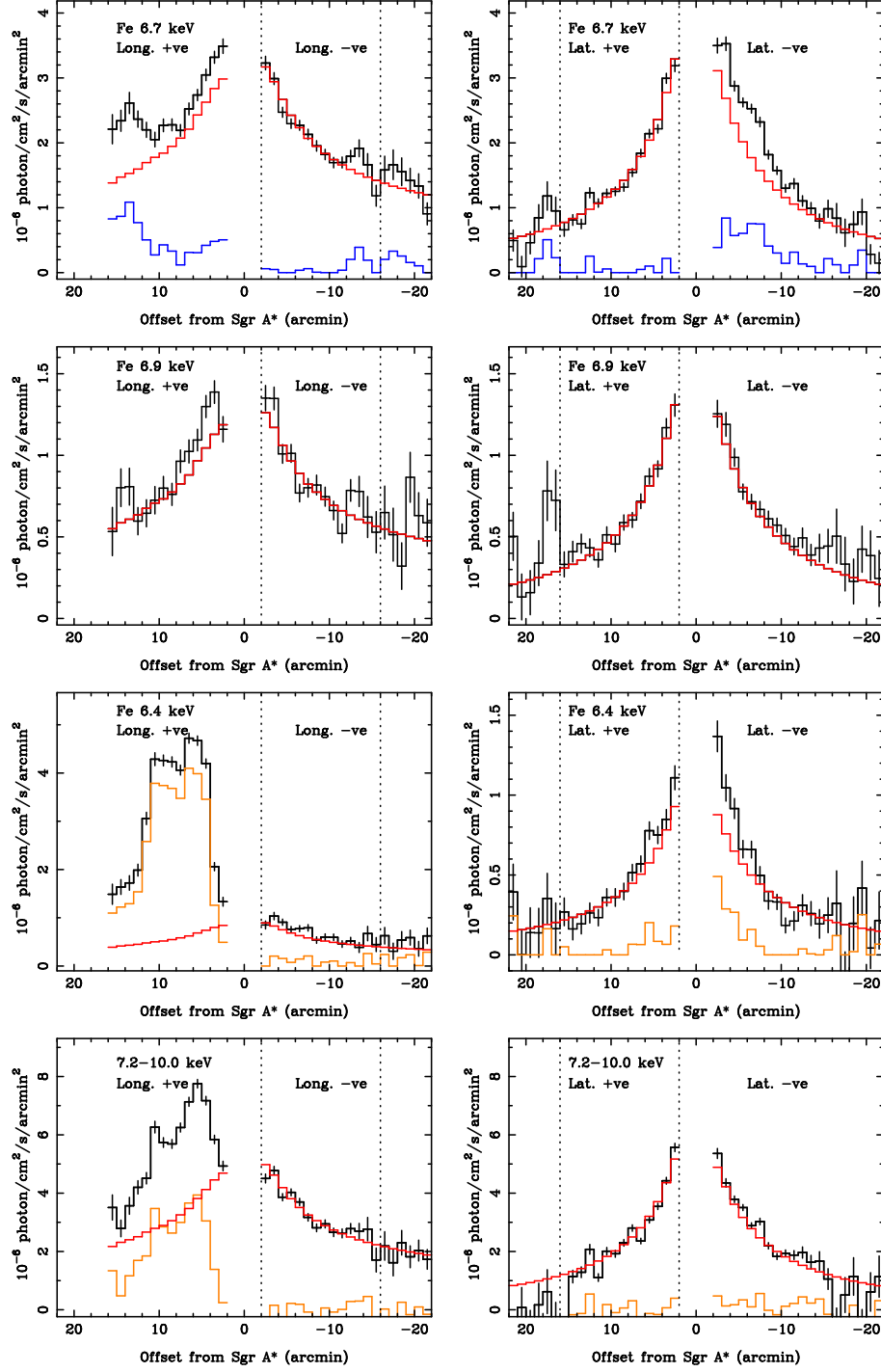
Figure 4. Spatial cuts through the GC images from the pn camera. The left-hand panels show the longitudinal cuts (where +ve offset is to the Galactic east of Sgr A*) and the right-hand panels show the latitudinal cuts (where +ve offset is to the Galactic north of Sgr A*). The spatial resolution is $1'$ along the cut direction. The cuts have a full width of $8'$ in the perpendicular direction. The black points and histograms represent the data. The best-fitting unresolved source model is shown as the red histogram. The data segments used to fit the source component are identified by the vertical dotted lines. *Upper panels:* Cuts through the 6.7-keV iron-line image. The blue histogram represents the residual 6.7-keV emission once the source component is subtracted (only +ve residuals are considered); this excess signal may be associated with the $kT \approx 1.5$ keV thermal emission component. *Upper-mid panels:* Cuts through the 6.9-keV iron-line image. *Lower-mid panels:* Cuts through the 6.4-keV iron-line image. The orange histogram represents the residual 6.4-keV emission once the contribution of the unresolved-sources is subtracted (only +ve residuals are considered); this excess signal is associated with the fluorescence of dense molecular clouds. *Lower panels:* Cuts through the 7.2–10 keV band image. The orange histogram represents the residual emission once the contribution of the unresolved-sources is subtracted (only +ve residuals are considered); this excess signal is associated with reflection from dense molecular clouds.

analysis of the softer thermal plasma emission will follow in a later publication (Heard & Warwick, *in preparation*).

3.2 Spatial distribution of the unresolved sources

As a means of investigating the spatial distribution of the unresolved source population, we have employed an empirical 2-d surface brightness model which can be matched to the available spatial information. We adopt a model in which the surface brightness, S, decreases as a power-law function of the angular offset θ (measured in arcmin) from Sgr A*. The observations demonstrate very clearly that the rate of decrease is faster perpendicular to the Galactic Plane than along the plane. We accommodate this by including an exponential fall-off with the latitudinal angle ϕ, where ϕ is measured with respect to the Galactic latitude of Sgr A*. The resulting model was:

$$S = N\theta^{-\alpha}exp(-\frac{|\phi|}{\phi_{sc}}) + S_{fg}, \qquad (1)$$

where the parameters N, α, and ϕ_{sc}, represent the normalisation of the power-law component, the power-law index, and latitudinal scale height (in arcmin), respectively. The surface brightness is presumed to peak at the position of Sgr A*, although in the model we actually constrained the power-law component interior to $\theta = 1'$ to the value at $1'$. The model also includes a constant foreground surface brightness S_{fg}. We set the latter equal to 10 per cent of the value of the variable component at $\theta = 12'$, $\phi = 0'$. The 10 per cent factor matches the decrease in surface brightness in the 6.7-keV Fe XXV Kα line measured by *Suzaku* as the offset from Sgr A* increases from $12'$ to $1°$ (Uchiyama et al. 2011). In the present analysis S_{fg} represents the contribution of sources outside of the central few hundred parsec, *i.e.,* sources located either in the Galactic bulge or Galactic disc (Hong et al. 2009; Uchiyama et al. 2011).

3.3 Modelling the spatial cuts

Longitudinal and latitudinal spatial cuts derived from the 6.7-keV, 6.9-keV, and 6.4-keV iron-line images and the very-hard 7.2–10 keV continuum image are shown in Fig. 4 (in all cases these are measurements from the pn camera). Hereafter, we use the shorthand: Long +ve; Long -ve; Lat +ve; and Lat -ve to identify the different segments of these cuts, as per the labelling in Fig. 4.

A rapid decline in the surface brightness as the distance from Sgr A* increases is evident in most cases (with the notable exception of the 6.4 keV and very-hard continuum measurements in the Long +ve region), with the rate of decline being somewhat faster in the latitudinal direction. In order to match our empirical 2-d surface brightness model to these data, we derived a set of model distributions in the format of the 1-d cuts, corresponding to an α versus ϕ_{sc} parameter grid. Here the process was: (i) construct a model image in our standard format for the specified α and ϕ_{sc}; (ii) apply the source spatial mask, thereby mimicking the filtering of the actual data; and (iii) determine the spatial cut distribution (as per §2.3).

We then selected the 6.7-keV and 6.9-keV line data pertaining to the two "cleanest" regions, namely the Long -ve and Lat +ve segments in the offset range $2'$–$16'$, for fitting.
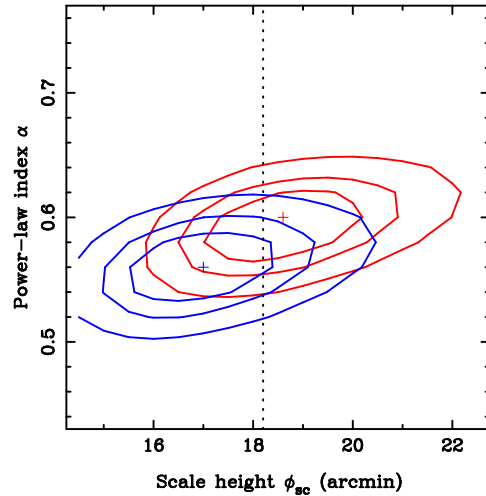
Figure 5. The variation of χ^2 as a function of the source model parameters, α and ϕ_{sc}. The contours represent the 68, 90, and 99 per cent confidence intervals. The results from the pn data are shown in red and those from the combined-MOS data in blue. The dashed vertical line is drawn at $18.2'$; this corresponds to the scale height of 45 pc reported for the Nuclear Stellar Disc by Launhardt et al. (2002) (see text).

The fitting process involved the determination of four free parameters, α, ϕ_{sc} and two normalisations (one for each line) via χ^2-minimisation. The results for the two "interesting" parameters, α and ϕ_{sc} are shown in the form of a 2-d confidence contour plot in Fig. 5. The best-fit values were $\alpha=0.60^{+0.02}_{-0.03}$ and $\phi_{sc}=18.6^{+1.6}_{-1.2}$ arcmin, respectively. The χ^2 for the best-fit was 109.0 for 54 degrees of freedom (dof), reflecting the fact that there is some (modest) scatter over and above the predicted level of the noise. Nevertheless, the best-fit model does account for the bulk of the 6.7-keV and 6.9-keV line emission in the Long -ve and Lat +ve regions (see Fig. 4). As a check we have repeated exactly the same analysis for the combined-MOS data. The derived constraints on the two model parameters α and ϕ_{sc} from the MOS are also shown in Fig. 5; the MOS results ($\alpha=0.56^{+0.03}_{-0.02}$ and $\phi_{sc}=17.0^{+1.4}_{-1.4}$ arcmin; $\chi^2 = 79.6$ for 54 dof) are fully consistent with those obtained from the pn channel, indicating that our modelling process is robust.

As a further test, using the best-fit values for α and ϕ_{sc} derived from the pn data, have also we fitted the Long -ve and Lat +ve cuts ($2'$–$16'$) for the 6.4-keV iron line and very-hard band data, which entailed determining the best-fit model normalisation for the respective bands[2]. The results, shown in Fig. 4, indicate that that the unresolved source model also accounts for the bulk of the emission measured in these bands within the fitted regions.

Finally the models derived for the Long -ve and Lat +ve regions were also extrapolated to the Long +ve and Lat -ve regions (with all the parameters including the normalisations fixed). Fig. 4 shows the results. In the Long +ve segment, the unresolved source model generally under-predicts

---

[2] In the case of the 7.2–10 keV band, we obtained our best result when we subtracted a constant offset from the cut data of 7.1×10^{-7} photon/cm^2/s/arcmin^2 - this may reflect the limitations of the background subtraction in this continuum band.

the observed signal. This is perhaps not surprising given that this is the region to the north-east of Sgr A*, where X-ray fluorescence and soft thermal emission are very prominent (Fig. 2 & 3). However, the model does provide quite a reasonable description of the 6.9-keV line emission in this region.

In the Lat -ve segment, there appears to be an enhancement in 6.7-keV line emission over and above the source model contribution. This excess extends out to an offset of $\sim 10'$ (~ 25 pc). There is some evidence for excess 6.4-keV emission in this same region, but in this case extending only to $\sim 5'$. Interestingly, *Chandra* data provide evidence of some unusual emission clumps to the south of Sgr A*, which arguably form part of a larger-scale bipolar feature (Baganoff et al. 2003; Morris et al. 2003). Plausibly, these are all elements of an extended structure linking back to the Sgr A East region (Heard & Warwick, 2012 , *in preparation*). Nevertheless, the source model again provides a good match to the 6.9-keV and very-hard band cuts in the Lat -ve region.

In summary, our modelling of the GC spatial cuts leads us to the conclusion that the X-ray emission observed in the 6–10 keV bandpass (encompassing three prominent iron lines Fe I Kα, Fe XXV Kα, and Fe XXVI Lyα at 6.4, 6.7, and 6.9 keV respectively plus a very-hard continuum), to a large extent follows a smooth, symmetric, centrally-concentrated spatial distribution consistent with an origin in unresolved point sources. There are two regions where additional emission components are clearly required. In the Long +ve region, X-ray fluorescence and reflection from dense molecular clouds is a major contributor to the 6.4-keV line emission and the very-hard continuum band. In this same region, the excess 6.7-keV line flux may be interpreted in terms of soft-thermal emission, with the lack of an associated excess at 6.9-keV constraining the temperature of the plasma to be less than a few keV. Excess 6.7 keV emission is also seen in the Lat -ve region, in a structure which may traced back to the central 10 pc region.

The next step was to investigate whether the spectral characteristics of the centrally-concentrated component are consistent with a putative origin in the integrated emission of low-luminosity sources. An indication of the spectral characteristics of this component is provided by the source model normalisations determined for each of the bands considered in Fig. 4. The normalisation of the source model for the 6.7-keV band relative to that measured in the 7.2–10 keV band implies an equivalent width for the 6.7-keV iron line of ≈ 630 eV (assuming the underlying continuum has a 7.5-keV thermal bremsstrahlung spectral form). Similarly, the source model normalisations measured for the 6.4-keV and 6.9-keV bands imply equivalent widths in excess of 200 eV for both lines. This characterisation of the source emission in terms of a hard continuum coupled with a trio of prominent iron lines is substantiated by the results of spectral fitting presented in the next section.

3.4 Modelling the X-ray spectra

The X-ray spectra measured by the pn camera in the four regions identified in Fig. 2 (which we again refer to as the Long +ve, Long -ve, Lat +ve, Lat -ve regions) are shown in

Fig. 6. In the spectral fitting of these data we have considered the three emission components discussed earlier (§3.1).

The first component represents the integrated emission from unresolved sources and was characterised in the spectral fitting as a `bremss` continuum with $kT = 7.5$ keV, plus Gaussian-line components corresponding to the Fe I Kα, Fe XXV Kα, and Fe XXVI Lyα lines. The intrinsic width of the 6.4-keV and 6.9-keV lines was fixed at 30 eV, in line with previous estimates of apparent line-widths in pn spectra (Capelli et al. 2012). In the case of the 6.7-keV He-like iron line, preliminary fitting of the Lat +ve spectrum indicated a best-fit value for the intrinsic width of ~ 55 eV, and in the subsequent spectral analysis the intrinsic width of this line was fixed at this value. Similarly the energies of the three iron lines were measured to be 6.41 ± 0.01 keV, 6.68 ± 0.01 keV, and 6.97 ± 0.01 keV, and subsequently fixed at these values. An Fe I Kβ line was included at an energy of 7.07 keV and width 30 eV with a normalisation tied to 11 per cent of that of the Fe I Kα line (Koyama et al. 2009).

The second emission component representing the fluorescence and reflection from dense molecular clouds was modelled as a power-law continuum with photon index Γ plus two Gaussian lines corresponding to neutral Fe Kα and Kβ (with parameters other than the normalisation of the Fe Kα line set as above).

Soft thermal emission constituted the final ingredient of the composite spectral model. Twin `apec` components with temperatures fixed at $kT_1 = 0.8$ keV and $kT_2 = 1.5$ keV were used to represent the likely complex temperature structure. In the spectral fitting the metal abundance was allowed to vary from region to region, but in all cases was tied across the two thermal components.

It was assumed that each of above components was subject to absorption. For the soft thermal emission we set $N_H = 6.5 \times 10^{22}$ cm^{-2}, in line with recent estimates of the soft X-ray absorption along the line-of-sight to the GC (e.g., Muno et al. 2006). In the case of the integrated emission of the unresolved sources and the reflection/scattering from molecular clouds, the absorption column density was increased to $N_H = 12 \times 10^{22}$ cm^{-2}, so as to include an additional contribution intrinsic either to the source spectra or the molecular cloud environment. Unfortunately the intrinsic absorption is rather poorly constrained due to the pervasive soft thermal emission, thus a value of 5.5×10^{22} cm^{-2} was eventually chosen so as to give reasonably consistent results across the four regions.

With all the elements of the composite spectral model in place[3], we first attempted to fit the spectra of the Lat +ve and Long -ve regions with the integrated source emission model (involving four free parameters, *i.e.,* the normalisations of the bremsstrahlung continuum and the three iron emission lines) together with a $kT = 0.8$ keV `apec` component (involving two further free parameters - the `apec` normalisation and metal abundance). This restricted model provided a good match to the observational data (Fig. 6)

---

[3] Our spectra model also included a power-law continuum with photon index $\Gamma = 1.4$, subject to an absorbing column density $N_H = 13 \times 10^{22}$ cm^{-2} with a normalisation matched to that of the CXB (Lumb et al. 2002; De Luca & Molendi 2004). However, the inclusion of this component had negligible impact on the spectral fitting results.
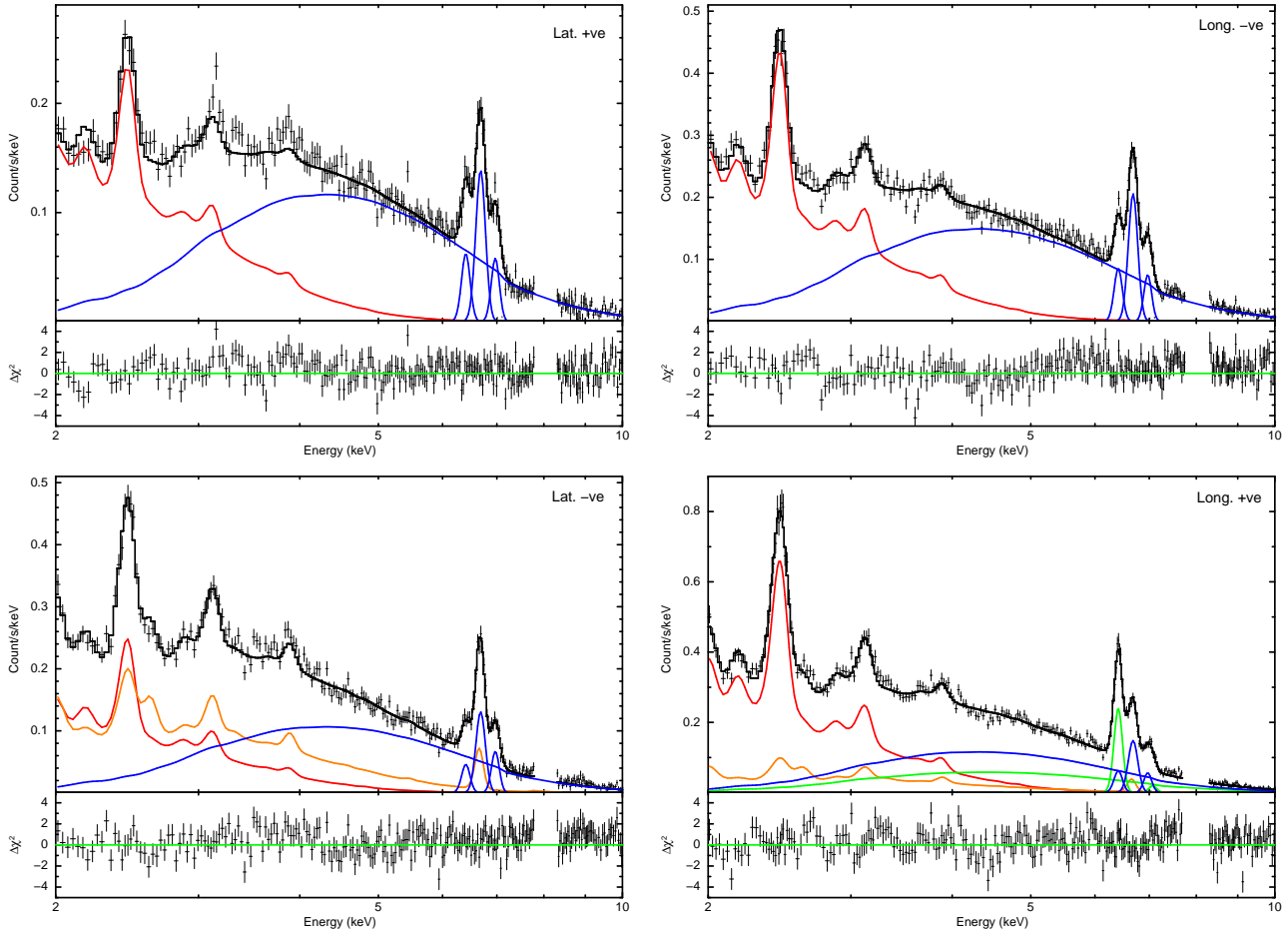
Figure 6. X-ray spectra measured by the pn camera in observation 0202670801 in four regions - *Upper-left panel:* the Lat +ve region; *Upper-right panel:* the Long -ve region; *Lower-left panel:* the Lat -ve region; *Lower-right panel:* the Long +ve region. Each panel shows the X-ray spectrum after background subtraction in the 2–10 keV band, excluding the region around the Cu Kα instrumental line. The best-fitting model and the fitting residuals are also shown. The contribution of different spectral components is illustrated by the different colour curves - *blue:* the 7.5 keV thermal bremsstrahlung continuum plus iron lines associated with unresolved sources; *green:* the fluorescent iron line and reflected continuum from dense molecular clouds; *red:* soft thermal emission with $kT = 0.8$ keV; *orange:* (relatively) soft thermal emission with $kT = 1.5$ keV.

with best-fitting parameters as listed in Table 5. Of particular note is the fact that the derived equivalent widths for each line are reasonably consistent across the two regions, and broadly in line with the expectations based on the spatial cuts analysis (§3.3). Based on our best-fitting unresolved source model, a 2–10 keV flux of 1.1×10^{-11} erg s^{-1} cm^{-2} has, on average, an associated 6.7-keV photon flux of 4.0×10^{-5} photon s^{-1} cm^{-2}.

In extending the spectral analysis to the Lat -ve region, it was necessary to introduce the hotter $kT = 1.5$ keV `apec` component into the fitting (thus accounting for the excess 6.7-keV iron line emission observed in this region - see §3.3). The best-fit model for this region is again illustrated in Fig. 6 and the best-fit parameter values tabulated in Table 5. Again the parameters for the integrated source emission are strikingly similar to those of the Lat +ve region.

Finally, for the Long +ve region we required the full composite spectral model, consistent with our earlier identification of this region as the most active of the four considered. Here the spectral-fitting approach was to fix the parameters of the unresolved-source emission model at those

obtained from the Long -ve region. The additional free-parameters were those quantifying the reflection from the molecular clouds (*i.e.,* the continuum normalisation and photon index) and the fluorescence (*i.e.,* the normalisation of the 6.4-keV line) Again, Fig. 6 and Table 5 summarise the results. The derived photon index of $\Gamma \approx 1.8$ is consistent with other recent estimates (Capelli et al. 2012). Similarly the inferred large equivalent width of the fluorescent line (~ 1.7 keV) is in line with published values (Ponti et al. 2010; Capelli et al. 2011, 2012).

An interesting result from Table 5 is the inferred variation in the metal abundance across the four regions, with values ranging from 0.5–2 $Z_\odot$. We measure the highest metal abundance to the north-east of Sgr A* (Long +ve), the site with the most recent supernova activity, which could have led to a localised enrichment of the thermal plasma. A *Suzaku* study of the GC X-ray emission in the same region determined the abundance to be in the range $\sim$ 1–2 $Z_\odot$ (Nobukawa et al. 2010), consistent with the current measurements.

In order to test the hypothesis that the integrated

Table 5. The best-fitting spectral parameters for the four regions.

Region	Lat +ve	Long -ve	Lat -ve	Long +ve
Unresolved source component				
$N_{\rm H}$ ($\times 10^{22}$ cm^{-2})	12	12	12	12
kT (keV)	7.5	7.5	7.5	7.5
$Norm.$ ($\times 10^{-3}$)	5.90 ± 0.09	6.93 ± 0.09	5.92 ± 0.19	6.93
$EW_{6.4}$ (eV)	236 ± 27	233 ± 23	188 ± 30	233
$EW_{6.7}$ (eV)	691 ± 37	781 ± 37	710 ± 58	781
$EW_{6.9}$ (eV)	296 ± 33	283 ± 27	366 ± 37	283
Reflection component				
$N_{\rm H}$ ($\times 10^{22}$ cm^{-2})	-	-	-	12
Γ	–	–	–	$1.8^{+0.2}_{-0.2}$
$Norm.$ ($\times 10^{-3}$)	-	-	-	$3.3^{+1.4}_{-1.0}$
$EW_{6.4}$ (eV)	-	-	-	1655 ± 80
Soft thermal plasma component				
$N_{\rm H}$ ($\times 10^{22}$ cm^{-2})	6.5	6.5	6.5	6.5
kT_1 (keV)	0.8	0.8	0.8	0.8
Norm. ($\times 10^{-2}$)	$9.6^{+1.0}_{-1.0}$	$11.2^{+1.1}_{-1.1}$	$5.7^{+1.0}_{-0.8}$	$8.6^{+1.5}_{-1.5}$
kT_2 (keV)	-	-	1.5	1.5
Norm. ($\times 10^{-2}$)	-	-	$2.7^{+0.3}_{-0.3}$	$0.81^{+0.24}_{-0.21}$
Z ($Z_\odot$)	$0.49^{+0.11}_{-0.09}$	$0.73^{+0.12}_{-0.10}$	$1.07^{+0.17}_{-0.14}$	$2.18^{+0.56}_{-0.39}$
χ^2/ν	1473.7/1422	1404.1/1414	1560.9/1423	1569.2/1407

source emission is largely due to magnetic CVs, we have employed the spectral model for intermediate polars (IPs) developed by Yuasa et al. (2010). This IP model has three free parameters: the white dwarf (WD) mass $M_{\rm WD}$; the relative iron abundance $Z_{\rm Fe}$, and a normalisation factor. When this spectral model was substituted for the thermal bremsstrahlung continuum and the associated lines at 6.7 keV and 6.9 keV (with the normalisation of the 6.4-keV line retained as a free parameter since the IP model does not include 6.4-keV iron line emission), we obtained an excellent fit to the data with a χ^2/ν value for the joint-fitting of the spectra for the Lat +ve and Long -ve regions of 2944.8/2849. The best-fitting values for the white dwarf mass and iron abundance were 0.49 ± 0.02 $M_\odot$ and 0.97 ± 0.05 $Z_\odot$. This estimate of the typical mass of a magnetic white dwarf in the GC is, in fact, very similar to that obtained by Yuasa et al. (2012) in their analysis of *Suzaku* XIS and HXD/PIN spectra pertaining to a set of Galactic bulge fields. However, as noted by these authors this mass estimate is very likely biased downwards by other types of CV, such as dwarf novae in quiescence, which have lower representative temperatures. Also the lack of spectral information above 10 keV in the current analysis, severely compromises the measurement of the effective temperature of the emission ($kT > 15$ keV), which directly impinges on the mass estimate. Nevertheless, the analysis does demonstrate that it is very plausible that the bulk of the emission seen above 5 keV in the *XMM-Newton* spectra is attributable to an unresolved source population dominated by magnetic CVs.

4 DISCUSSION

4.1 The low-luminosity X-ray source population at the Galactic Centre

Our spatial and spectral analysis confirms the view that much of the hard X-ray emission observed within 20′ of Sgr A* can be attributed to the integrated emission of unresolved low-luminosity X-ray sources. The spectral characteristics of this component - a hard continuum (with $kT \sim 7.5$ keV when modelled as thermal bremsstrahlung) plus three iron lines (Fe I Kα, Fe XXV Kα, and Fe XXVI Lyα) of relatively high equivalent width - places a tight constraint on the nature of the underlying population. These spectral properties rule-out a significant contribution from most classes of coronally-active stars and binaries or from young stellar objects (Muno et al. 2003). High-mass and low-mass X-ray binaries (HMXBs and LMXBs) represent the most X-ray luminous X-ray population within the Galactic disc and bulge (Muno et al. 2003; and references therein), but it seems highly unlikely that very low-luminosity versions of such sources exist in sufficient numbers in the GC to explain the observations, although some quiescent LMXBs do seem to have the requisite hard spectra (e.g., Wijnands et al. 2005).

Currently, the leading candidate for the unresolved source population is magnetic CVs (Muno et al. 2004a; Laycock et al. 2005), which in principle include both polars and IPs. Although the spectra of these subclasses of CV can both be characterised as multi-temperature thermal plasmas, the plasma temperatures of polars are lower due to enhanced cyclotron cooling (*e.g.,* Cropper et al. 1998) and it is the IPs which likely dominate the hard (> 10 keV) emission seen from the GC (Yuasa et al. 2012) and, correspondingly,

make the largest contribution to the key iron-line tracers. Nearby, well-studied magnetic cataclysmic variables typically have 2–10 keV X-ray luminosities in the range from 10^{31} – 10^{34} erg s^{-1} (*e.g.,* Sazonov et al. 2006), although the true low-luminosity bound for the population may be at least one, and possibly two, orders of magnitude fainter (Revnivtsev et al. 2009). A key question for the unresolved source model is whether there are sufficient magnetic CVs in the GC to account for the bulk of the observed hard X-ray luminosity.

As a starting point, we have determined the integrated X-ray luminosity, L_X, of the unresolved source component. For this purpose, we first measured the normalisation of the empirical surface brightness model, when fitted to the Long -ve and Lat +ve segments of the spatial cuts pertaining to the 4.5–6 keV pn images (noting that in these regions, the unresolved sources appear to provide the dominant contribution to the 4.5–6 keV flux). Next we converted pn count s^{-1} in the 4.5–6 keV band to X-ray flux in the full 2–10 keV band (via the spectral model of the unresolved source component discussed previously), and applied the necessary scaling factors to transform the surface brightness model units to X-ray luminosity per square parsec. Finally, we determined the radial surface-brightness distribution from an image derived from the model[4]. The result is shown in the upper-left panel of Fig.7. Integrating this distribution from $2'$–$20'$ (which corresponds to a projected offset of 4.6–46 pc at the GC), we obtain $L_X \approx 2.0 \times 10^{36}$ erg s^{-1} as the total integrated (2–10 keV) X-ray luminosity of the unresolved sources (below a source detection threshold of $L_X \approx 10^{33}$ erg s^{-1}).

The next step was to consider the GC stellar mass contained within this region. Here we use the same mass-model prescription as Muno et al. (2006), who in turn use parameters obtained from an analysis of *NIR* maps by Launhardt et al. (2002)[5]

Within the central few hundred parsecs of the Galaxy, two major stellar distributions have been identified: the Nuclear Stellar Cluster (NSC) and the Nuclear Stellar Disc (NSD).

The NSC has a mass density, which varies with radius R as:

$$\rho = \frac{\rho_c}{1 + (R/R_c)^{n_1}}. \tag{2}$$

For $R < 6$ pc, $\rho_c = 3.3 \times 10^6$ M$_\odot$pc^{-3}, $R_c = 0.22$ pc, and $n_1 = 2$. For $6 < R < 200$ pc, $n_1 = 3$, R_c remains the same and ρ_c must be adjusted so that the profile is continuous at $R = 6$ pc.

The mass distribution of the NSD can be modelled as a power-law plus exponential function,

$$\rho = \rho_d R^{-n_2} \exp(-|z|/z_d). \tag{3}$$

For $R < 120$ pc, $\rho_d = 300$ M$_\odot$pc^{-3}, $n_2 = 0.1$, and $z_d = 45$ pc. For $120 < R < 220$ pc, becomes $n_2 = 3.5$ with z_d unchanged; ρ_d must be adjusted so that the function is continuous for $n_2 = 3.5$. Beyond 220 pc this disc component is assumed to cut-off rapidly.

The other components of the mass-model discussed by Muno et al. (2006) are the Galactic bulge and disc. However, these are not considered here, since they contribute only to the constant term in our empirical surface brightness model (on the angular scales considered), which was not included in the derivation of the integrated luminosity.

We integrated the mass distributions in the NSC and NSD components along a set of lines-of-sight to give the stellar mass per square parsec on a 2-d grid of positions centred on Sgr A*. From this 2-d distribution we then determined the average stellar-mass density within circular annuli of width $1'$ as a function of radial offset in the range $2'$–$20'$. The result is shown in the upper-right panel of Fig.7, which displays both the individual contributions of the NSC and NSD and their sum. It is evident that the NSD provides the dominant mass contribution for offset angles greater than a few arcmin and that the NSC component becomes insignificant outside $\sim 10'$.

The scale height for the NSD of 45 pc reported by Launhardt et al. (2002), based on IRAS 100 μm dust measurements, corresponds to $18.2'$ at the distance of the GC assumed by these authors. This is in excellent agreement with the scale height inferred from the X-ray observations (see Fig. 5) and consistent with the fact that the NSD is the major contributor to the stellar mass within the region sampled by the X-ray observations.

The X-ray emissivity per unit stellar mass can be readily determined from the ratio of the curves presented in the upper-left and upper-right (total mass) panels of Fig. 7. The result is shown in the lower-left panel of Fig. 7. A smooth trend is apparent with offset angle, with the inferred emissivity varying from $\approx 5 \times 10^{27}$ erg s^{-1} M$_\odot^{-1}$ at $20'$ up to almost twice this value at $2'$.

By way of comparison Sazonov et al. (2006) constructed an X-ray luminosity function for faint sources in the local neighbourhood, from which they determined the total X-ray emissivity for CVs and active binaries (that is sources associated with the old stellar population) to be $\sim (3.1 \pm 0.8) \times 10^{27}$ erg s^{-1} M$_\odot^{-1}$ in the 2–10 keV band, with CVs contributing roughly one-third of this total. More recently, using a deep *RXTE*/PCA scan across the Galactic Plane at $l_{II} \sim +18.0°$, Revnivtsev & Molkov (2012) calculate the 2–10 keV emissivity in the GRXE to be $(3.0 \pm 0.3) \times 10^{27}$ erg s^{-1} M$_\odot^{-1}$. Moving closer to the GC, from a *Chandra* deep-field observation targeted at the inner Galactic bulge ($l_{II} \sim 0.113°$, $b_{II} \sim$ -1.424°), Revnivtsev et al. (2011) estimate the 2–10 keV X-ray emissivity to be $(2.4 \pm 0.4) \times 10^{27}$ erg s^{-1} M$_\odot^{-1}$. Finally from a similar *Chandra* study based on deep-field data taken within $1'$-$4'$of Sgr A*, Revnivtsev et al. (2007) derived an X-ray emissivity value of $\sim (8.5 \pm 4.3) \times 10^{27}$ erg s^{-1} M$_\odot^{-1}$ (corrected to a GC distance of 8 kpc). Here the large error stems from uncertainty in the GC mass model - see the discussion below.

Taken as a whole, the published measurements provide evidence of an up-lift in the X-ray emissivity per unit stellar

---

[4] We use circular annuli of width $1'$. Hence the derived radial distribution represents an average over latitude and longitude.
[5] Muno et al. (2006) adopt the same parameters values as Launhardt et al. (2002) despite the fact that the original analysis was based on a GC distance of 8.5 kpc. However, as noted by Launhardt et al. (2002), in practice, such scaling corrections are typically much smaller than the uncertainties in the parameter determinations. In the present paper we employ the same mass-model formulation as Muno et al. (2006), along with the assumption of a GC distance of 8 kpc.
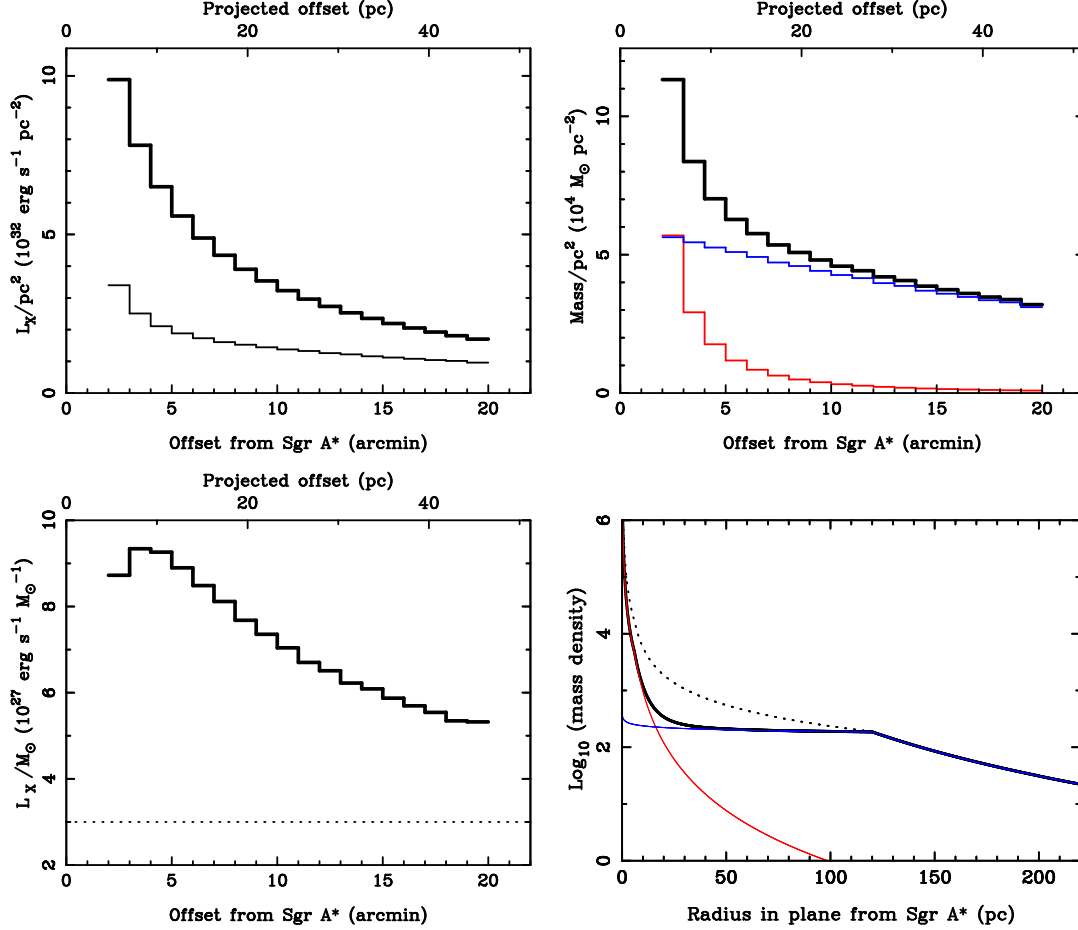
Figure 7. *Upper-left panel:* Variation of the 2–10 keV X-ray surface brightness (in units of 10^{32} erg s^{-1} pc^{-2}) as a function of the angular offset from Sgr A*. The thick and thin black lines are the luminosity per square parsec derived from the X-ray images and predicted from the mass-model respectively. *Upper-right panel:* Projected mass density (in units of 10^4 M$_\odot$ pc^{-2}) in the GC showing the contribution of the NSC (red), the NSD (blue), and their sum (black). *Lower-left panel:* The inferred X-ray emissivity per unit stellar mass (in units of 10^{27} erg s^{-1} M$_\odot^{-1}$) as a function of the angular offset from Sgr A*. The dotted line is the "base-level" X-ray emissivity which is representative of measured GRXE values. *Lower-right panel:* The variation in the stellar mass density on the plane (in units of M$_\odot$ pc^{-3}) for the GC region as a function of the distance (in pc) from Sgr A*. The solid black curve represents the sum of the NSC (red) and the NSD (blue) components in the Muno et al. (2006) model. The dotted black curve is the mass-model (sum of the NSC and NSD components) inferred on the basis of the assumption that the X-ray emissivity in the region is 3×10^{27} erg s^{-1} M$_\odot^{-1}$.

mass of the unresolved source population within < 1 deg of Sgr A*, which is substantiated by our current results.

Two interpretations are possible for the upward trend in the X-ray emissivity per unit stellar mass within the central 100-pc zone evident in Fig. 7. The first is that some characteristic of the underlying source population is changing in tandem with the stellar density. If we assume the "base-level" X-ray emissivity of the old stellar population is roughly 3.0×10^{27} erg s^{-1} M$_\odot^{-1}$ (*i.e.*, a value representative of the GRXE excluding the GC) and apply this scaling to the projected mass distribution (Fig. 7, top-left panel), then the observed X-ray luminosity shows a factor ~ 2 enhancement relative to this base-level. Conceivably the binarity of stellar population, and hence the incidence of magnetic CVs, might be dependent on the stellar density. Alternatively, the contribution from other source types (*e.g.,* extreme RSCVn binaries) might rise within 50 pc of Sgr A* in a fashion analogous to that inferred for the central stellar cusp (Sazonov et al. 2012). The nucleus of M31 presents an

interesting comparator. Within $1'$ of the centre of M31, the incidence of luminous X-ray sources ($L_X < 10^{36}$ erg s^{-1}) increases more rapidly than might be predicted from the K-band light (Voss & Gilfanov 2007a), a result which has been interpreted in terms of the dynamical formation of LMXBs within a dense stellar environment (Voss & Gilfanov 2007b). At the distance of M31, $1'$ corresponds to a linear extent of 200 pc, a scale-size not dissimilar to the extent of the NSC and NSD components discussed above. Plausibly, dynamical processes may have given rise to a higher incidence of X-ray emitting CVs and active binaries within the central 100-pc region, than that pertaining in the Galaxy as a whole.

An alternative explanation of the observed upward trend in the X-ray emissivity per unit stellar mass and the implied enhanced X-ray luminosity of the central 100-pc region, is that the mass model we have employed is inaccurate. In fact a number of authors have noted that the uncertainties in the current mass model, including the relative scaling of the NSC and NSD components, may be as

high as a factor of ~ 2 (Launhardt et al. 2002; Muno et al. 2006; Revnivtsev et al. 2007).

We have investigated what changes in the mass distribution are implied by our measurements, if we make the assumption that the X-ray emissivity within the GC region is constant. Bearing in mind that we are dealing with quantities measured in projection on the plane of the sky (*i.e.,* integrated along the line-of-sight through the whole nuclear region), we have necessarily sought a representative solution rather than a unique one. In that context, we find that the upward trend in the emissivity can be counteracted by steepening, the power-law function describing the decrease with radius of the NSD mass density within $R < 120$ pc; specifically the power-law index must be changed from $n_2 = 0.1$ to $n_2 = 1.2$. The total GC mass profile which results in a roughly constant X-ray emissivity of 3.0×10^{27} erg s^{-1} M$_\odot^{-1}$ between $2'$–$20'$, is shown in the lower-right panel of Fig. 7. We note that compared to the current mass model (Launhardt et al. 2002; Muno et al. 2006), additional mass (roughly a factor 2) is required within 10-100 pc of Sgr A*; however, it is unclear whether this is appropriately assigned to the NSC, the NSD or to a combination of both. In summary, this analysis demonstrates that X-ray tracers may eventually provide a very effective way of constraining the stellar mass distribution in the GC; of course, this is subject to the caveat that we need to better understand the nature of GC X-ray source population and the evolutionary influences to which it has been subject.

Finally we may use the estimates of this section to illustrate just how extreme the environment is at the centre of the Galaxy. If we take the stellar mass density to be $\sim 10^3$ M$_\odot$ pc^{-3} (the value at ~ 20 pc on the plane in our revised mass model), then the base-level X-ray emissivity per unit stellar mass assumed above implies an X-ray volume emissivity of 3×10^{30} erg s^{-1} pc^{-3}. If a typical magnetic CV in this region has an X-ray luminosity of $L_X \sim 10^{30}$ erg s^{-1}, consistent with the faint end of the source distribution probed in *Chandra* deep-field observations (Revnivtsev et al. 2009), then the volume density of magnetic CVs is ~ 3 pc^{-3}. However, only ~ 5 per cent of all CVs are thought to be IPs (Ruiter et al. 2006), so the projected number density of all types of CVs rises to 60 pc^{-3}, compared to the inferred local density of just $\sim 10^{-5}$ pc^{-3} (Warner 1995; Schwope et al. 2002).

4.2 Absence of very-hot diffuse thermal plasma in the GC

The GRXE can be traced along the Galactic Plane from $|l_{\mathrm{II}}| \sim 90°$ through to the GC, where its surface brightness reaches a maximum (Koyama et al. 1986, 1989; Revnivtsev et al. 2006). In recent years the debate as to whether this feature is due predominantly to the presence of a truly diffuse very-hot ($kT \sim 7.5$ keV) thermal plasma or due to the integrated emission of point sources, has inexorably swung in favour of the latter interpretation.

A key recent result in the context of the origin of the emission from the GC was the discovery that in a deep *Chandra* observation at $(l_{\mathrm{II}}, b_{\mathrm{II}} = +0.08°, -1.42°)$, more than ~ 80 per cent of the continuum and line emission around 6.7 keV could be resolved into point sources (Revnivtsev et al. 2009). Also detailed spectral analysis of *Suzaku* observations

in the Galactic bulge region, suggests that virtually all of the unresolved X-ray emission can be explained in terms of the integrated emission of point sources (Yuasa et al. 2012).

In this paper, we have investigated the distribution of X-ray emission in the region between $2'$ and $20'$ from Sgr A* in a variety of bands, encompassing three iron-line tracers and also the very-hard 7.2–10 keV continuum. We find that in many regions the emission in these bands follows a smooth, symmetric centrally-concentrated spatial distribution. Furthermore, to within a factor of 2, the observed surface brightness distribution matches the projected mass distribution in the old stellar population in the GC, specifically that in the Nuclear Stellar Disc component (Launhardt et al. 2002; Muno et al. 2006). We interpret this as strong support for the conjecture that the observed emission is predominantly the integrated emission of unresolved point sources.

Excluding the central $2'$, where the Sgr A East SNR, the Central Cluster, and other features combine to produce a complex morphology (Baganoff et al. 2003; Muno et al. 2004b), and also a few regions dominated by individual X-ray binaries or other bright sources (*e.g.,* the Arches Cluster), we identify two regions within $20'$ of the GC where the underlying glow of point sources is confused by additional emission components. The first is the north-east region where X-ray fluorescence and reflection from dense molecular clouds gives rise to a strong signal in the 6.4-keV iron-line and the very-hard continuum bands. Excess emission at 6.7-keV can be seen in this north-east region and, also in a second "anomalous" region to the south of Sgr A*. In both cases we interpret the 6.7-keV excess as a concentration of soft thermal emission with temperature ~ 1.5 keV. The key point is that within this overall setting there is no requirement for any excess *very-hard* thermal emission which might be attributed to a residual diffuse GRXE component.

In a recent paper, Uchiyama et al. (2011) used *Suzaku* measurements to trace the distribution of iron-K emission from the GC proper through to regions of the inner Galactic Plane ($|l_{\mathrm{II}}| = 1°$ − $10°$). Similar to the current analysis, these authors compared the spatial variation of the Fe XXV Kα line with a stellar mass distribution model. They found that when the X-ray emissivity per unit stellar mass was fixed at the value required to explain the observed emission outside of $|l_{\mathrm{II}}| \sim 1.5°$, then the X-ray emission observed within $1°$ was 3.8 times under-predicted. They concluded that either a new source population with extremely strong Fe XXV Kα emission was required in the GC or that the majority of hard GC X-ray emission must originate in a truly diffuse optically-thin thermal plasma. In the present paper we argue that the X-ray emissivity in the GC is roughly a factor 2 higher than estimates pertaining to the local Galaxy and Galactic Plane (Sazonov et al. 2006; Revnivtsev & Molkov 2012). A possible explanation of these different estimates of the degree to which the GC X-ray emissivity is enhanced (3.8x as opposed to 2x) is that Uchiyama et al. (2011) use a scaling for their Galactic disc component, taken from Muno et al. (2006), which is based on a total mass in the Galactic disc of 10^{11} M$_\odot$. However, as noted by Hong et al. (2009) this is likely to be an overestimate of the total *stellar mass* in the disc; for example Robin et al. (2003) quote a value of 2.2×10^{10} M$_\odot$. Whatever the actual degree of enhancement of the X-ray emissivity in the central 100-pc region, we hold to the view that

the observed spatial distribution and spectral properties of this component are best explained in terms of the integrated emission of unresolved sources.

5   CONCLUSIONS

We have used the extensive set of observations available in the *XMM-Newton* archive to make mosaiced images of the central 100 pc × 100 pc region of our Galaxy in a variety of broad and narrow bandpasses within the 2–10 keV energy range.

Using three iron-K lines (Fe I Kα at 6.4 keV, Fe XXV Kα at 6.7 keV and Fe XXVI Lyα at 6.9 keV) as tracers, we decompose the GC X-ray emission into three distinct components. The first of these components is the integrated emission of unresolved point sources with 2–10 keV X-ray luminosity $L_X < 10^{33}$ erg s^{-1}. The second is the fluorescent line emission and the reflected continuum from dense molecular material. The third is the soft diffuse emission from thermal plasma in the temperature range, $kT \approx 0.8$–1.5 keV. We show that the spatial distribution and spectral properties of the GC X-ray emission (excluding the central 2′ region and a few other regions confused by luminous sources) can, to a good approximation, be described in terms of these three components.

A key finding is that unresolved sources account for much of the observed emission in 6–10 keV band, including the iron-line emission. We find that the surface brightness of this component falls off as $\sim \theta^{-0.6}$, where θ is the angular offset from Sgr A*, coupled with a latitudinal scale height factor $\phi_{sc} = 18.6^{+1.6}_{-1.2}$ arcmin.

We assume that the unresolved sources are associated with the old stellar population of the Galaxy, which can be traced in the GC through the NIR light, on the basis of which, a 3-d mass model has been derived by Launhardt et al. (2002). According to Launhardt et al. (2002) there are two major stellar structures within the central 100 pc of the Galaxy, namely the Nuclear Stellar Cluster (NSC) and the Nuclear Stellar Disc (NSD). When we project these two components of the mass-model onto the 2-d plane of sky, we find that it is the NSD which dominates the region sampled by the X-ray measurements. The X-ray surface brightness distribution (as parameterised above) rises more rapidly with decreasing θ than the mass-model prediction. One interpretation is that the 2–10 keV X-ray emissivity increases from $\approx 5 \times 10^{27}$ erg s^{-1}M$_\odot^{-1}$ at 20′ up to almost twice this value at 2′. Alternatively, some refinement of the mass model may be required. Specifically if we assume the X-ray emissivity in the central region is similar to that pertaining to GRXE as a whole (*i.e.*, $\sim 3 \times 10^{27}$ erg s^{-1}M$_\odot^{-1}$), then roughly a factor of two additional mass is required within 10–100 pc of Sgr A*. However, it is unclear whether this applies to the NSC, the NSD, or a combination of both components.

When we set $n_2 = 1.2$ in the NSD model and revise the model normalisation so as to conserve the total mass in the NSD within our 2′–20′ field of view, we obtain an X-ray emissitivity per unit stellar mass of $\approx 6.5 \times 10^{27}$ erg s^{-1}M$_\odot^{-1}$. This is within a factor 2 of other estimates of this quantity based on the local X-ray luminosity function and studies of the GRXE component outside of the GC region.

The unresolved hard X-ray emitting source population, on the basis of spectral comparisons, is most likely dominated by magnetic cataclysmic variables, primarily intermediate polars. By way of example, we use the X-ray observations to estimate that there are 60 CVs (of all types) per cubic parsec at a radial distance of 20 pc from Sgr A*. This is close to seven orders of magnitude over the local CV number density.

A further major finding of our work is that our composite emission model, encompassing the three components described above, provides a sufficiently good description of the observations so as to rule out any substantial additional source of hard X-ray luminosity in the GC. It has long been conjectured that a significant fraction of the hard X-ray emission from the GC originates in very-hot (~ 7.5 keV) *diffuse* thermal plasma. Within our modelling framework, the only way of accommodating a substantial contribution of this nature, is within the emission component we attribute to unresolved sources. However, the properties of the latter, namely the smooth, symmetrical, centrally-concentrated spatial distribution, an X-ray emissivity reasonably in accord with local estimates, and an X-ray spectrum matching that of intermediate polars, would seem to exclude the diffuse, very-hot thermal plasma hypothesis as a viable option.

REFERENCES

Baganoff F. K. et al., 2003, *ApJ*, 591, 891

Blackburn J. K., 1995, in Astronomical Society of the Pacific Conference Series, Vol. 77, Astronomical Data Analysis Software and Systems IV, R. A. Shaw, H. E. Payne, & J. J. E. Hayes, ed., p. 367

Capelli R., Warwick R. S., Porquet D., Gillessen S., Predehl P., 2011, *A&A*, 530, A38

Capelli R., Warwick R. S., Porquet D., Gillessen S., Predehl P., 2012, *A&A*, 545, A35

Crocker R. M., Jones D. I., Aharonian F., Law C. J., Melia F., Oka T., Ott J., 2011, *MNRAS*, 413, 763

Cropper M., Ramsay G., Wu K., 1998, *MNRAS*, 293, 222

Cropper M., Wu K., Ramsay G., Kocabiyik A., 1999, *MNRAS*, 306, 684

De Luca A., Molendi S., 2004, *A&A*, 419, 837

Ghez A. M. et al., 2008, *ApJ*, 689, 1044

Gillessen S., Eisenhauer F., Trippe S., Alexander T., Genzel R., Martins F., Ott T., 2009, *ApJ*, 692, 1075

Hellier C., Mukai K., 2004, *MNRAS*, 352, 1037

Hong J. S., van den Berg M., Grindlay J. E., Laycock S., 2009, *ApJ*, 706, 223

Kaneda H., Makishima K., Yamauchi S., Koyama K., Matsuzaki K., Yamasaki N. Y., 1997, *ApJ*, 491, 638

Koyama K., Awaki H., Kunieda H., Takano S., Tawara Y., 1989, *Nature*, 339, 603

Koyama K. et al., 2007a, *PASJ*, 59, 245

Koyama K. et al., 2007b, *PASJ*, 59, 221

Koyama K., Maeda Y., Sonobe T., Takeshima T., Tanaka Y., Yamauchi S., 1996, *PASJ*, 48, 249

Koyama K., Makishima K., Tanaka Y., Tsunemi H., 1986, *PASJ*, 38, 121

Koyama K., Takikawa Y., Hyodo Y., Inui T., Nobukawa M., Matsumoto H., Tsuru T. G., 2009, *PASJ*, 61, 255

Launhardt R., Zylka R., Mezger P. G., 2002, *A&A*, 384, 112

Laycock S., Grindlay J., van den Berg M., Zhao P., Hong J., Koenig X., Schlegel E. M., Persson S. E., 2005, *ApJL*, 634, L53

Lumb D. H., Warwick R. S., Page M., De Luca A., 2002, *A&A*, 389, 93

Morris M. et al., 2003, Astronomische Nachrichten Supplement, 324, 167

Morris M., Serabyn E., 1996, *ARA&A*, 34, 645

Muno M. P. et al., 2004a, *ApJ*, 613, 1179

Muno M. P. et al., 2003, *ApJ*, 589, 225

Muno M. P. et al., 2004b, *ApJ*, 613, 326

Muno M. P., Baganoff F. K., Brandt W. N., Morris M. R., Starck J.-L., 2008, *ApJ*, 673, 251

Muno M. P. et al., 2009, *ApJS*, 181, 110

Muno M. P., Bauer F. E., Bandyopadhyay R. M., Wang Q. D., 2006, *ApJS*, 165, 173

Murakami H., Koyama K., Sakano M., Tsujimoto M., Maeda Y., 2000, *ApJ*, 534, 283

Nobukawa M., Koyama K., Tsuru T. G., Ryu S. G., Tatischeff V., 2010, in American Institute of Physics Conference Series, Vol. 1269, American Institute of Physics Conference Series, Tanihara I., Ong H. J., Tamii A., Kishimoto T., Kajino T., Kubono S., Shima T., eds., pp. 154–159

Park S., Muno M. P., Baganoff F. K., Maeda Y., Morris M., Howard C., Bautz M. W., Garmire G. P., 2004, *ApJ*, 603, 548

Ponti G., Terrier R., Goldwurm A., Belanger G., Trap G., 2010, *ApJ*, 714, 732

Revnivtsev M., Sazonov S., Churazov E., Forman W., Vikhlinin A., Sunyaev R., 2009, *Nature*, 458, 1142

Revnivtsev M., Sazonov S., Forman W., Churazov E., Sunyaev R., 2011, *MNRAS*, 414, 495

Revnivtsev M., Sazonov S., Gilfanov M., Churazov E., Sunyaev R., 2006, *A&A*, 452, 169

Revnivtsev M., Vikhlinin A., Sazonov S., 2007, *A&A*, 473, 857

Revnivtsev M. G., Molkov S. V., 2012, *MNRAS*, 424, 2330

Robin A. C., Reylé C., Derrière S., Picaud S., 2003, *A&A*, 409, 523

Ruiter A. J., Belczynski K., Harrison T. E., 2006, *ApJL*, 640, L167

Sazonov S., Revnivtsev M., Gilfanov M., Churazov E., Sunyaev R., 2006, *A&A*, 450, 117

Sazonov S., Sunyaev R., Revnivtsev M., 2012, *MNRAS*, 420, 388

Schödel R. et al., 2002, *Nature*, 419, 694

Schwope A. D., Brunner H., Buckley D., Greiner J., Heyden K. v. d., Neizvestny S., Potter S., Schwarz R., 2002, *A&A*, 396, 895

Smith R. K., Brickhouse N. S., Liedahl D. A., Raymond J. C., 2001, *ApJL*, 556, L91

Strüder L. et al., 2001, *A&A*, 365, L18

Sunyaev R., Churazov E., 1998, *MNRAS*, 297, 1279

Tsuboi M., Handa T., Ukita N., 1999, *ApJS*, 120, 1

Turner M. J. L. et al., 2001, *A&A*, 365, L27

Uchiyama H., Nobukawa M., Tsuru T., Koyama K., Matsumoto H., 2011, *PASJ*, 63, 903

Voss R., Gilfanov M., 2007a, *A&A*, 468, 49

Voss R., Gilfanov M., 2007b, *MNRAS*, 380, 1685

Wang Q. D., Dong H., Lang C., 2006, *MNRAS*, 371, 38

Wang Q. D., Gotthelf E. V., Lang C. C., 2002, *Nature*, 415, 148

Warner B., 1995, Cataclysmic Variable Stars. (Cambridge: *Cambridge University Press*)

Warwick R. S., Turner M. J. L., Watson M. G., Willingale R., 1985, *Nature*, 317, 218

Watson M. G. et al., 2009, *A&A*, 493, 339

Wijnands R., Heinke C. O., Pooley D., Edmonds P. D., Lewin W. H. G., Grindlay J. E., Jonker P. G., Miller J. M., 2005, *ApJ*, 618, 883

Worrall D. M., Marshall F. E., 1983, *ApJ*, 267, 691

Yamasaki N. Y. et al., 1997, *ApJ*, 481, 821

Yamauchi S., Ebisawa K., Tanaka Y., Koyama K., Matsumoto H., Yamasaki N. Y., Takahashi H., Ezoe Y., 2009, *PASJ*, 61, 225

Yuasa T., Makishima K., Nakazawa K., 2012, *ApJ*, 753, 129

Yuasa T., Nakazawa K., Makishima K., Saitou K., Ishida M., Ebisawa K., Mori H., Yamada S., 2010, *A&A*, 520, A25

This paper has been typeset from a TeX/ LaTeX file prepared by the author.